

# Characterization of a tagged $\gamma$ -ray beam line at the DAΦNE Beam Test Facility

P.W. Cattaneo<sup>\*g</sup>, A. Argan<sup>a</sup>, F. Boffelli<sup>g</sup>, A. Bulgarelli<sup>e</sup>, B. Buonomo<sup>u</sup>, A.W. Chen<sup>c,d</sup>, F. D'Ammando<sup>v</sup>, L. Foggetta<sup>\*\*d</sup>, T. Froyland<sup>b,d</sup>, F. Fuschino<sup>e</sup>, M. Galli<sup>h</sup>, F. Gianotti<sup>e</sup>, A. Giuliani<sup>c</sup>, F. Longo<sup>f,t</sup>, M. Marisaldi<sup>e</sup>, G. Mazzitelli<sup>u</sup>, A. Pellizzoni<sup>f</sup>, M. Presti<sup>l</sup>, G. Pucella<sup>m</sup>, L. Quintieri<sup>u</sup>, A. Rappoldi<sup>g</sup>, M. Tavani<sup>a,b</sup>, M. Trifoglio<sup>e</sup>, A. Trois<sup>r</sup>, P. Valente<sup>i</sup>, E. Vallazza<sup>f</sup>, S. Vercellone<sup>s</sup>, A. Zambra<sup>c</sup>, G. Barbiellini<sup>f,t</sup>, P. Caraveo<sup>c</sup>, V. Cocco<sup>a</sup>, E. Costa<sup>a</sup>, G. De Paris<sup>a</sup>, E. Del Monte<sup>a</sup>, G. Di Cocco<sup>e</sup>, I. Donnarumma<sup>a</sup>, Y. Evangelista<sup>a</sup>, M. Feroci<sup>a</sup>, A. Ferrari<sup>d,q</sup>, M. Fiorini<sup>c</sup>, C. Labanti<sup>e</sup>, I. Lapshov<sup>a</sup>, F. Lazzarotto<sup>a</sup>, P. Lipari<sup>i</sup>, M. Mastropietro<sup>j</sup>, S. Mereghetti<sup>c</sup>, E. Morelli<sup>e</sup>, E. Moretti<sup>f</sup>, A. Morselli<sup>k</sup>, L. Pacciani<sup>a</sup>, F. Perotti<sup>c</sup>, G. Piano<sup>a,b,k</sup>, P. Picozza<sup>b,k</sup>, M. Pilia<sup>l</sup>, G. Porrovecchio<sup>a</sup>, M. Rapisarda<sup>m</sup>, A. Rubini<sup>a</sup>, S. Sabatini<sup>a,b</sup>, P. Soffitta<sup>a</sup>, E. Striani<sup>b,k</sup>, V. Vittorini<sup>a,b</sup>, D. Zanello<sup>i</sup>, S. Colafrancesco<sup>n</sup>, P. Giommi<sup>n</sup>, C. Pittori<sup>n</sup>, P. Santolamazza<sup>n</sup>, F. Verrecchia<sup>n</sup>, L. Salotti<sup>o</sup>

<sup>a</sup>INAF/IASF-Roma, I-00133 Roma, Italy

<sup>b</sup>Dip. di Fisica, Univ. Tor Vergata, I-00133 Roma, Italy

<sup>c</sup>INAF/IASF-Milano, I-20133 Milano, Italy

<sup>d</sup>CIFS-Torino, I-10133 Torino, Italy

<sup>e</sup>INAF/IASF-Bologna, I-40129 Bologna, Italy

<sup>f</sup>INFN Trieste, I-34127 Trieste, Italy

<sup>g</sup>INFN-Pavia, I-27100 Pavia, Italy

<sup>h</sup>ENEA-Bologna, I-40129 Bologna, Italy

<sup>i</sup>INFN-Roma La Sapienza, I-00185 Roma, Italy

<sup>j</sup>CNR-IMIP, Roma, Italy

<sup>k</sup>INFN Roma Tor Vergata, I-00133 Roma, Italy

<sup>l</sup>Dip. di Fisica, Univ. Dell'Insubria, I-22100 Como, Italy

<sup>m</sup>ENEA Frascati, I-00044 Frascati (Roma), Italy

<sup>n</sup>ASI Science Data Center, I-00044 Frascati(Roma), Italy

<sup>o</sup>Agenzia Spaziale Italiana, I-00198 Roma, Italy

<sup>p</sup>Osservatorio Astronomico di Trieste, Trieste, Italy

<sup>q</sup>Dip. Fisica, Università di Torino, Torino, Italy

<sup>r</sup>INAF-Osservatorio Astronomico di Cagliari, localita' Poggio dei Pini, strada 54, I-09012 Capoterra, Italy

<sup>s</sup>INAF-IASF Palermo, Via Ugo La Malfa 153, I-90146 Palermo, Italy

<sup>t</sup>Dip. Fisica Univ. di Trieste, I-34127 Trieste, Italy

<sup>u</sup>INFN Lab. Naz. di Frascati, I-00044 Frascati(Roma), Italy

<sup>v</sup>INAF-IRA Bologna, Via Gobetti 101, I-40129 Bologna, Italy

---

## Abstract

---

\*Corresponding author

\*\*Now at LAL-CNRS, F-91898 Orsay, France

Email address: Paolo.Cattaneo@pv.infn.it (P.W. Cattaneo)

At the core of the AGILE scientific instrument, designed to operate on a satellite, there is the Gamma Ray Imaging Detector (GRID) consisting of a Silicon Tracker (ST), a Cesium Iodide Mini-Calorimeter and an Anti-Coincidence system of plastic scintillator bars. The ST needs an on-ground calibration with a  $\gamma$ -ray beam to validate the simulation used to calculate the energy response function and the effective area versus the energy and the direction of the  $\gamma$  rays. A tagged  $\gamma$ -ray beam line was designed at the Beam Test Facility (BTF) of the INFN Laboratori Nazionali di Frascati (LNF), based on an electron beam generating  $\gamma$  rays through bremsstrahlung in a position-sensitive target. The  $\gamma$ -ray energy is deduced by difference with the post-bremsstrahlung electron energy [1]-[2]. The electron energy is measured by a spectrometer consisting of a dipole magnet and an array of position sensitive silicon strip detectors, the Photon Tagging System (PTS). The use of the combined BTF-PTS system as tagged photon beam requires understanding the efficiency of  $\gamma$ -ray tagging, the probability of fake tagging, the energy resolution and the relation of the PTS hit position versus the  $\gamma$ -ray energy. This paper describes this study comparing data taken during the AGILE calibration occurred in 2005 with simulation.

*Key words:* Electron and positron beam; Photon beam; Position-sensitive detectors; bremsstrahlung  
*PACS:* 41.75.Fr, 41.85.p, 29.40.Gx, 41.60.-m

---

## 1. Introduction

AGILE (Astro-rivelatore Gamma a Immagini LEggero) is a Small Scientific Mission of the Italian Space Agency (ASI), dedicated to high-energy astrophysics. It combines two co-aligned imaging detectors operating respectively in the X and  $\gamma$ -ray bands with large Field of Views (FoV). The Silicon Tracker (ST), at the core of the AGILE satellite, is designed to detect and image  $\gamma$  rays in the 30 MeV-50 GeV energy range [3]-[4]-[5]-[6].

The on-ground calibration of an astronomical instrument is important for the interpretation of its results. The goal is to reproduce in laboratory, under controlled condition, the response of the instrument in flight. This task requires a tagged photon beam with position, direction and energy of each photon known with a precision better than the instrument resolution. The realization of such a beam turns out to be a challenging endeavour. The Beam Test Facility (BTF) in the DAΦNE collider complex at the INFN Laboratori Nazionali di Frascati (LNF) [7], was the elected site for realizing the tagged photon beam exploiting bremsstrahlung in a thin target and performing the calibration. Preliminary results on the calibration of the AGILE ST has been presented in Ref.[8] and will be subject of a future paper.

This paper presents the experimental setup, a detailed Monte Carlo study of the system and the comparison with the experimental results collected during the calibration.

## 2. The experimental setup

The experimental setup is a complex system consisting of the BTF  $e^-$  beam, the target to generate bremsstrahlung photons, the spectrometer magnet and the detector

to measure the energy of post-bremsstrahlung electrons. The various subsystems are described in the following with the convention that  $y$  is the coordinate perpendicular to the BTF line plane,  $x$  the one transverse to the beam at the target in the BTF line plane and  $z$  is the one along the beam at the target, that is the direction of the bremsstrahlung photons.

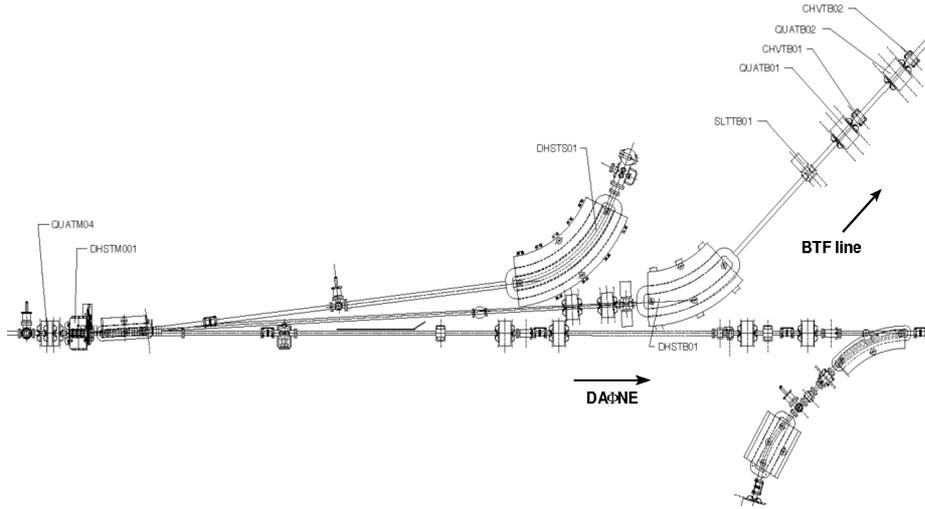


Figure 1: The initial section of the BTF transfer line.

## 2.1. The electron beam

The  $e^-$ s used for generating the photon beam are delivered by the BTF. The BTF is fed by the DAΦNE complex that provides  $e^\pm$  under carefully controlled condition with predefined multiplicity.

### 2.1.1. The Beam Test Facility (BTF)

For the ST calibration we used the BTF in the DAΦNE collider complex at LNF, which includes a LINAC at high  $e^+/e^-$  currents, an accumulator of  $e^+/e^-$  and two storage rings at 510 MeV. The  $e^+/e^-$  beam from the LINAC is directed into the accumulation ring to be subsequently extracted and injected in the Main Ring. When the system injector does not transfer the beams to the accumulator, the beam from LINAC can be extracted and transported in the test beam area through a dedicated transfer line: the BTF line (Fig. 1). The BTF can provide a collimated beam of  $e^+/e^-$  in the energy range 20-750 MeV with a pulse rate of 50 Hz. The pulse duration can vary from 1 to 10 ns and the average number of  $e^-$  per bunch  $\overline{N}_e$  ranges from 1 to  $10^{10}$  [7]-[9]-[10]. The BTF can be operated in two ways:

- *LINAC mode*: operating when DAΦNE is off, with a tunable energy between 50 MeV and 750 MeV and an efficiency around 0.9.

- *DAΦNE mode*: operating when DAΦNE is on, with a fixed energy at 510 MeV and an efficiency around 0.6.

The extracted electrons are transported to the BTF hall, where the final section is located (Fig. 2); the experimental equipment under test is positioned at the exit of the spectrometer magnet DHSTB02. All or part of the equipment can be mounted under vacuum continuing the beam line or, alternatively, the beam line can be terminated with a thin window and the equipment mounted in air.

In spite of some disadvantage from the point of view of background, this last option was adopted with a 0.5 mm Be window because of the difficulties in implementing an extended vacuum line incorporating all the required equipment.

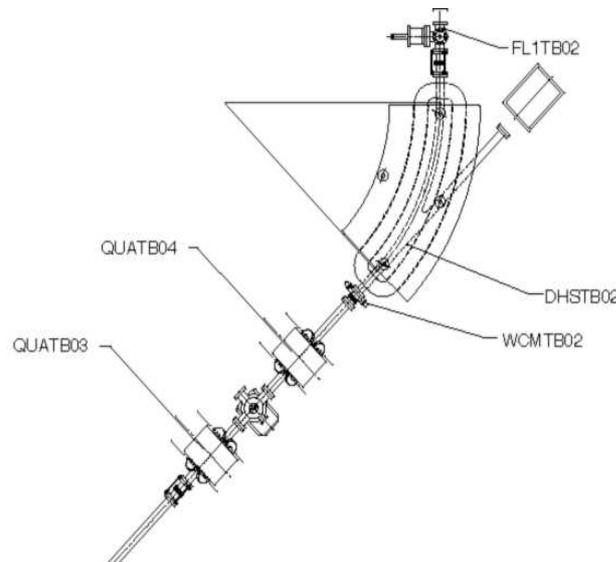


Figure 2: The final section of the BTF transfer line including the last spectrometer magnet DHSTB02.

### 2.1.2. $e^-$ multiplicity per bunch

The calibration of the ST should be ideally performed in a single-photon regime, avoiding simultaneous multi-photon production to reproduce the astrophysical conditions. Multi-photon events should ideally be identified and rejected otherwise they will bias the counting statistics.

On the other hand, bremsstrahlung is a continuous process and multi-photon generation (with photon energy  $E_\gamma$  above a given threshold) is possible also when a single  $e^-$  crosses the target. The fraction of multi-photon events is approximately proportional to the single-photon emission probability. That implies the need of a compromise between the photon beam intensity and the single-photon beam purity.

Considering that the target thickness was constrained by the availability of the hardware, by the need to guarantee full detection efficiency of the beam electrons and by

the need to measure electrons twice both in the  $x$  and  $y$  directions for studying the beam size and divergence, the only free parameter is the  $e^-$  multiplicity per bunch. Another constraint is the limited time available for the calibration campaign and the request of calibrating many different ST geometrical configurations. That puts a lower limit to the required photon flux and therefore on the  $e^-$  multiplicity per bunch. In DAΦNE mode with 5  $e^-$ /bunch the fraction of multi-photon events having  $E_\gamma > 20$  MeV can be estimated to be  $\approx 10\%$  by the formulae in the Appendix. This uncertainty is greater than the accuracy requirement on the effective area measurements. On the other hands, the DAΦNE mode with 1  $e^-$ /bunch is consistent with the accuracy requirements but the time necessary to collect enough statistics is incompatible with the time available for the calibration. The ST cross-section for photons with  $E_\gamma < 20$  MeV is not negligible and thus the fraction of interacting secondary photons will be larger than the numbers calculated in the Appendix. Taking into account the above considerations, the best configuration for ST performance and calibration would be with 1  $e^-$ /bunch, but the flux requirement forced to select the configuration with  $\approx 3 e^-$ /bunch.

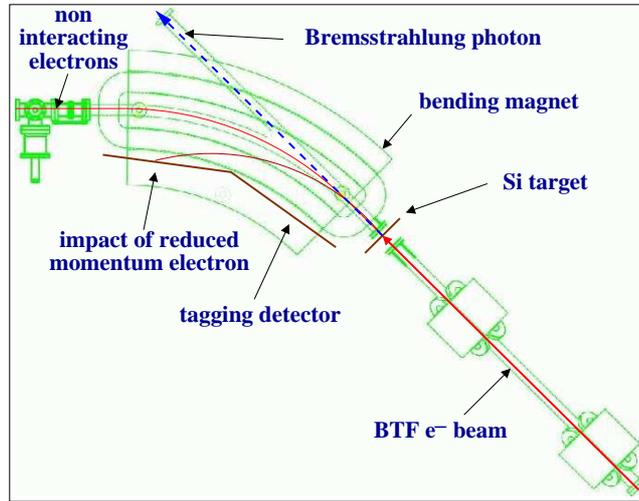


Figure 3: A schematic view of the  $\gamma$ -ray line: the target, the spectrometer magnet and the PTS.

## 2.2. The bremsstrahlung target

Photons in the energy range relevant for the ST are produced by bremsstrahlung of electrons in a target; subsequently a magnet bends away the electrons while the  $\gamma$  rays can travel towards the AGILE instrument (see Fig.3).

The bremsstrahlung target consists of two pairs of silicon single sided micro-strip detectors of area  $8.75 \times 8.75 \text{ cm}^2$  and  $410 \mu\text{m}$  thick, each including 768 strips with  $114 \mu\text{m}$  pitch. Only every other strip is read, so that each target detector has 384 readout channels with  $228 \mu\text{m}$  readout pitch. Each pair measures separately the  $x$  and  $y$  coordinates transverse to the beam. A spatial resolution  $\sigma \leq 114/\sqrt{12} \mu\text{m} \approx 33 \mu\text{m}$  is expected;

the cluster size is often limited to one strip and therefore the resolution is limited by the strip pitch.

The target has two roles: to measure the coordinate and the direction of the electrons and to cause the emission of bremsstrahlung photons. The target detectors are positioned along the beam direction between the last focusing magnet (QATB04 in Fig.2) and the spectrometer magnet (DHSTB02 in Fig.2). The  $x$  measuring ones are the first and the third, positioned respectively at 5.45 cm and 7.20 cm downstream the Be window, while the  $y$  measuring ones are the second and the fourth, positioned respectively 6.45 cm and 8.20 cm downstream the Be window.

At the electron energy most used during calibration,  $E_e = 463$  MeV, the contribution to beam divergence due to Coulomb Multiple Scattering in each target detector is evaluated under the Gaussian approximation from Ref. [11] as  $\approx 2.0$  mrad.

### 2.3. The photon tagging system (PTS)

The spectrometer magnet, visible in Fig.2-Fig.3-Fig.4, generates a dipolar field along the  $y$  direction over an angular range of  $45^\circ$ . In between the two magnet poles, there is a pipe made of stainless steel with rectangular section. It is composed of a straight section ('photon pipe') along which the bremsstrahlung  $\gamma$  rays travel to the ST and a curved section ('electron pipe') defining the trajectory for  $e^-$ s bent by the magnetic field.

The pipe is hollow with an air filled inner section with size  $5.50 \times 3.50$  cm<sup>2</sup>, its wall thickness is 0.35 cm. The magnetic field in the volume between the poles that includes the 'electron pipe' is assumed constant with strength  $B = 0.9$  T when  $E_e = 463.0$  MeV, corresponding to a curvature radius  $R = 172.0$  cm.

The equipment for the detection of the  $e^-$ s that lost energy in the target was developed and installed inside the spectrometer magnet by our team: the Photon Tagging System (PTS). It consists of 12 micro-strip silicon detectors positioned on the internal walls of the spectrometer magnet (see Fig.2, Fig.3 and Fig.4) grouped into two modules of six detectors each, located into two hollow rectangular aluminum boxes few mm thick. In each module, the detectors are located along a straight segment and therefore follow only approximately the curved section of the 'electron pipe'. The area of each detector is  $11.86 \times 2.00$  cm<sup>2</sup> with thickness  $410 \mu\text{m}$  and is subdivided in 1187 strips with  $100 \mu\text{m}$  pitch. Only every third strip is read resulting in 384 readout strips per detector and 4608 in total.

Between each pair of consecutive detectors inside a module, there is a gap  $\approx 6$  mm wide that is effectively a dead area. A larger gap  $\approx 2.0$  cm wide is present between the two modules that contributes to the dead area as well. Electronic noise gives a small contribution compared to the signals from  $e^-$  amounting to  $\approx 2$  keV that is of little relevance for the measurements. Depending on the energy loss in the target, the electrons impinge on different strips. The correlation in time between the signals of the  $e^-$  in the target and in the PTS tags the photon; the position on the PTS measures the photon energy.

The trigger for reading out the target and PTS data is given by the delayed LINAC pre-trigger; it is read out independently from the ST data. This point has great relevance for the following analysis.

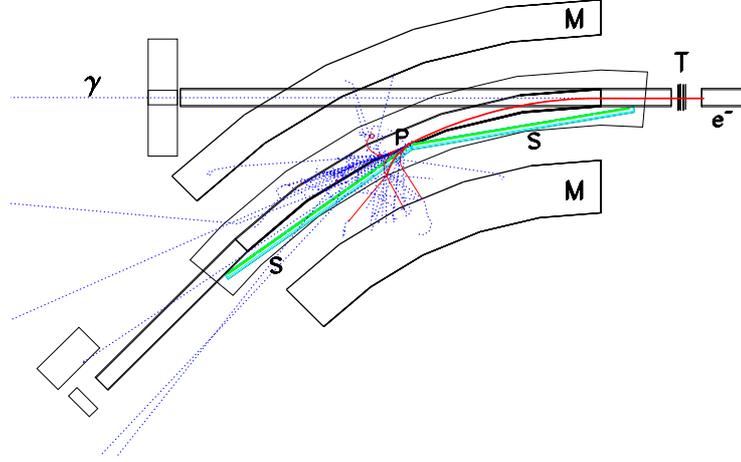


Figure 4: Geometry of the spectrometer magnet M drawn in GEANT3 including the PTS detectors S displayed with an  $e^-$  (entering from the right) irradiating a  $\gamma$  ray in the target T and hitting the PTS at P. Photons are represented by dashed (blue) lines and electrons by solid (red) lines. In this event the  $\gamma$  ray energy is  $\approx 75$  MeV.

### 3. The Monte Carlo simulation

A proper characterization of the BTF requires a careful comparison of the data with a detailed Monte Carlo simulation. The simulation is realized using the GEANT3 package [12]. The simulation incorporates a description of the electron beam delivered by the accelerator complex with beam parameters determined partly from design values and partly from measurements. The number of  $e^-$  per bunch  $N_e$  can be fixed to an integer value or can follow a Poisson distribution averaged at any real value  $\overline{N}_e$ .

The material distribution of the bremsstrahlung target and of the spectrometer is simulated in detail. The target and the pipe can be simulated in air or in vacuum in various configurations. The default configuration is the one actually used during data taking with the target and the pipe in air.

The interactions of electrons and photons are driven by the GEANT3 routines with the possibilities of switching on and off the relevant physics processes like Coulomb Multiple Scattering, bremsstrahlung, Compton scattering, pair creation for all or only for some of the materials. This option turned out to be very useful in understanding the behaviour of the BTF/PTS system. The energy cuts for the  $e^\pm$  and photons are kept at the minimum allowed by the program (100 keV). A gauge of the quality of these cuts is the average energy loss of a minimum ionizing particles crossing a  $\approx 400 \mu\text{m}$  thick silicon layer comparable to a target detector or a ST layer thickness: it is  $\approx 100$  keV. This level of precision is required to simulate spurious hits in the target and in the ST that can affect the measurement.

The digitization simulation in the silicon micro-strip detectors is based on a simpli-

fied model: the charge released in the volume below each strip is collected by the strip without accounting for diffusion and charge trapping. Exploiting the capacitive coupling [13], the charges collected on all strips are fed into the readout strips with appropriate coefficients as described in [3]. The noise is simulated simply adding a Gaussian distributed charge on each strip around a cluster; the width is determined by the data and amount to  $\approx 2$  keV.

The  $e^-$  beam is generated inside the last straight section of the accelerator  $\approx 5$  cm upstream the target with a beam spot of elliptical shape with a 2D Gaussian distribution, with angular divergences perpendicular to the beam generated according two separate Gaussian distributions and with a Gaussian distributed momentum spread. The momentum spread is provided by the DAΦNE staff, while the other beam parameters are directly measured.

### 3.1. The simulated photon beam

The photon beam directed to the ST is simulated through the interaction of the  $e^-$  beam with the target. The photon generation is due to the bremsstrahlung effect and follows Eq.2 in the Appendix. This formula shows an approximate  $1/E_\gamma$  dependency, that is a power spectrum with index  $\approx -1$ . More precisely, a fit of Eq.2 in the interval  $0.05 - 1.00$  with a power spectrum returns an index  $\approx -1.2$ .

The simulated energy spectrum of the most energetic  $\gamma$  rays reaching the ST (but not necessarily interacting with it) is shown in Fig. 5 with a power spectrum fit returning an index  $\approx -1.2$  as expected by the analytical formula. The number of  $e^-$ s per bunch is set to  $N_e = 1$  without Poisson fluctuation. The same result is obtained when  $\bar{N}_e = 3.5$  with Poisson fluctuation. This result is not obvious because of the energy dependent interactions along the path that could change the spectrum, that turn out to be small.

Another important element that characterizes the beam is the fraction of multi-photon events. Because in an astrophysical environment there are no such events, they must be considered background and must be minimized. If an event has two or more photons with energy above the detection threshold in the ST (about few tens of MeV), they can interact simultaneously in the ST. The reconstruction software, designed for the astrophysical environment, is not fit to identify such events and will most likely fail or return incorrect energy and direction. The percentage fraction of multi-photon events above a threshold is shown in Fig.6. Even for events with  $\bar{N}_e = 3.5$ , the fraction is not larger than a few % even for  $E_\gamma$  as small as 10 MeV. Therefore their contribution to errors in the measurement of the ST performances is at most of comparable size.

A related but somehow different issue is the number of low energy photons, say  $E_\gamma < 10$  MeV, accompanying a photon in the ST energy range ( $E_\gamma > 30$  MeV). This photons are not enough energetic to convert in a  $e^+e^-$  pair detectable in the ST, but they can interact in coincidence with a photon of higher energy generating spurious hits that can influence the proper reconstruction of the event.

## 4. Results and discussion

The analysis of the target and the PTS data allows the validation of the Monte Carlo simulation required to correlate the  $\gamma$ -ray energy and the PTS hit position.

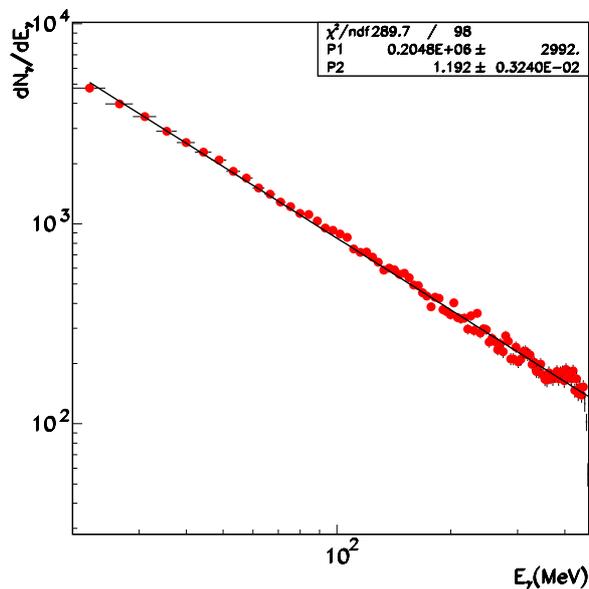


Figure 5: Spectrum of the  $\gamma$ -ray beam reaching the ST fit with a power law  $\alpha/E^\beta$ .

#### 4.1. The bremsstrahlung target data

The analysis of the target data starts from looking for strips above a threshold, then neighbouring strips are grouped into clusters. The cluster coordinate is obtained calculating its centroid by weighting each strip coordinate with the charge collected. Ideally, each cluster should signal a hit of one  $e^-$  in a target detector and the passage of each  $e^-$  should be signaled by one hit in each target detector. In practice there is the possibility of inefficiency in the detection of  $e^-$  hits, noise hits, multiple clusters due to a single  $e^-$  and single clusters on the same target detector associated to multiple  $e^-$ s. The efficiency of the hit searching algorithm is measured by selecting the events with one hit on three target detectors and zero on the fourth. This number is to be compared with the events with one hit on each target detector. With the available statistic, no event satisfies this requirement, so that the efficiency is basically 100%. The fraction of noise induced hits can be estimated by requiring one hit on one target detector and zero hit on the others. Also in this case, no event satisfies this requirement and therefore the fraction of noisy hits is basically 0%. Particularly interesting samples are the 0-cluster events, where no cluster is detected in the target, and the 1-cluster ones, where one cluster per target detector is detected. For the considerations detailed above, the first sample can be safely associated to events with 0- $e^-$  events; even these events are triggered because the target signal is not required by the trigger logic. The 1-cluster sample mostly overlaps with 1- $e^-$  events and is used in the following for characterizing the beam. The main goal of these measure-

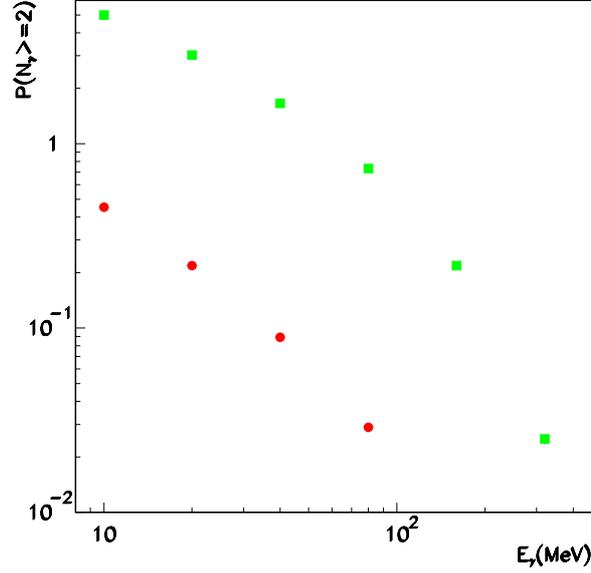


Figure 6: Probabilities (in %) of multi-photon events versus  $E_\gamma$  threshold for  $N_e = 1$  (fixed, red dots) and  $\bar{N}_e = 3.5$  (Poisson distributed, green squares).

ments is inferring the beam properties to be used in the Monte Carlo generation.

#### 4.1.1. Beam sizes

The beam sizes are measured only with 1-cluster sample. The beam profiles using the first  $x$  and  $y$  measured coordinates in the target are shown in the top row of Fig.7 with the results of Gaussian fits superimposed. Using the second  $x$  and  $y$  measured coordinates in the target gives compatible beam sizes. The beam sizes are  $\sigma_x \approx 1.5$  mm and  $\sigma_y \approx 0.5$  mm with a significant non Gaussian tail in  $y$ . This numbers are representative but subject to significant variations for different runs, due to changes in the beam setting.

#### 4.1.2. Beam divergences

Angular divergences are measured using the 1-cluster sample. The estimator is the difference between the cluster coordinates  $(x_i, y_i), i \in (1, 2)$  on the target divided by their distance  $d_{x(y)}$

$$\begin{aligned} s_x &= (x_2 - x_1)/d_x \\ s_y &= (y_2 - y_1)/d_y \end{aligned} \quad (1)$$

In Fig.7 (bottom row) the distributions of  $s_x$  and  $s_y$  are shown. The Gaussian fit returns  $\sigma(s_x) \approx 5.7$  mrad and  $\sigma(s_y) \approx 4.2$  mrad.

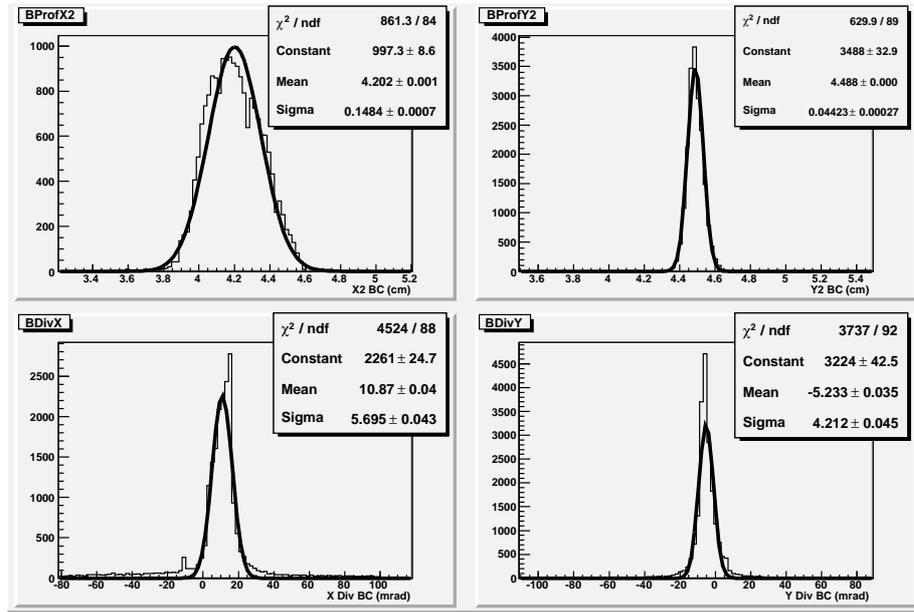


Figure 7: Beam parameters at  $E_e = 463$  MeV measured on data: x profile (top left), y profile (top right), x divergence (bottom left), y divergence (bottom right).

The beam divergences are, especially in y, smaller than those presented in Ref. [10]. That is due to an optimized setting of the accelerator slits for this particular application. The measured values for both the sizes and the divergences of the beam are fed into the Monte Carlo generator to reproduce the experimental distributions as shown in Fig.9.

#### 4.1.3. $e^-$ multiplicity

The  $e^-$  multiplicity of the BTF beam is one of the most important parameters required for an appropriate simulation of the photon beam. As discussed in Sect.2.1.2 the average of the Poisson distributed  $e^-$  multiplicity is tuned by the accelerator staff. It is nevertheless important to monitor the  $e^-$  multiplicity versus time to assess the reliability of the assumed multiplicity and its stability in time. The monitoring is possible by analyzing the hit multiplicity on the target. The  $e^-$  multiplicity is expected to follow a Poisson distribution with average  $\mu$

$$P_\mu(n) = \frac{\mu^n}{n!} e^{-\mu}$$

where  $\mu$  can be estimated from the fraction of 0- $e^-$  events given by  $P_\mu(0) = e^{-\mu}$ , that is  $\mu = -\log(P_\mu(0))$ .

Another estimation is obtained from the ratio of 1- $e^-$  events with multi- $e^-$  events

$$f_{12} = \frac{\mu e^{-\mu}}{\sum_{n>=2} \frac{\mu^n}{n!} e^{-\mu}}$$

If  $f_{12}$  is measured, this relation can be inverted numerically to obtain  $\mu$ . As previously mentioned the  $0\text{-}e^-$  events are readily identified as events with 0-cluster events, while the  $1\text{-}e^-$  sample largely overlaps with 1-cluster events. In order to study  $e^-$  multiplicity variation, events can be grouped in subsets of 1000 events with a sufficiently small statistical error. The estimated  $e^-$  multiplicity is plotted versus the event time for two calibration runs in Fig.8.

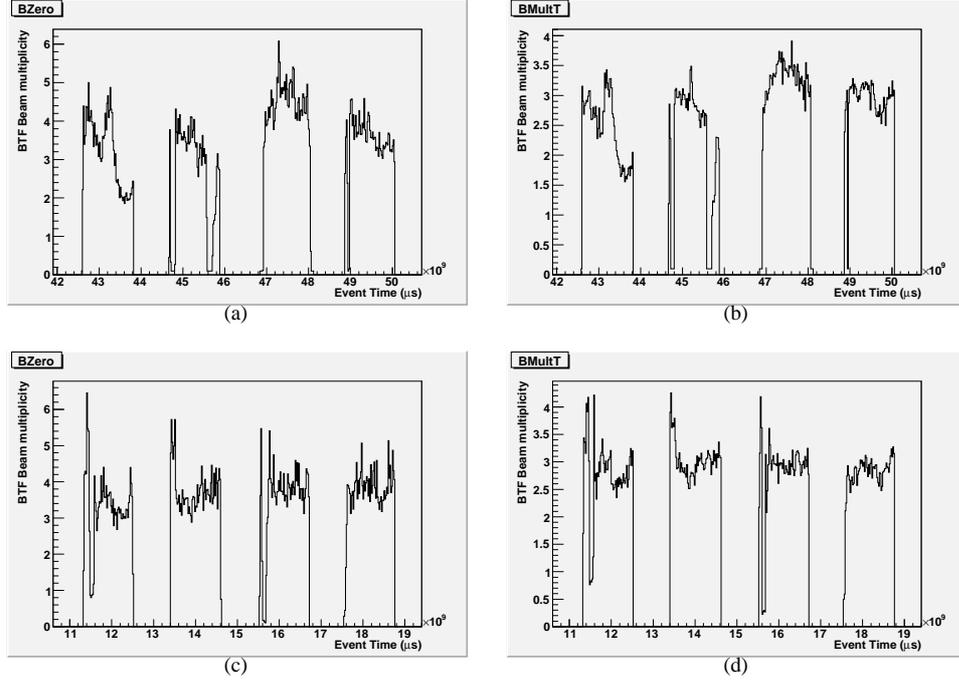


Figure 8: Estimation of  $e^-$  multiplicity with the  $0\text{-}e^-$  (left) and  $1\text{-}e^-$  (right) samples in the runs 2328 (top), 2566 (bottom).

These results show a broad agreement with the expected  $e^-$  multiplicity but also a quasi-periodic duty cycle of beam on-off. When beam is on, there are occasional spikes and sometimes smoother variations. The estimations from  $f_{12}$  is somehow lower than that from  $0\text{-}e^-$  events. That is expected if the chance that a multi- $e^-$  event appears as a 1-cluster event is higher than the reverse. That is what is expected for a narrow beam with some chance of overlapping hits from different  $e^-$ s.

#### 4.1.4. Beam simulation and comparison with data

The data contained from the target are used to tune the Monte Carlo simulation of the beam. The relevant parameters are the coordinates of the beam center, the widths of the beam spot, the beam divergences, the  $e^-$  multiplicity and the noise. The measurements are performed on the target while the parameters of the beam in the

Monte Carlo generator are generated upstream (see Sect. 4.1). These parameters may differ because of the spread of the uncollimated beam and of the multiple scattering along the path.

Nevertheless the simulation guarantees that the beam widths at the origin of the Monte Carlo generator show no significant difference with those measured on the target. Therefore the measured widths  $\sigma_x$  and  $\sigma_y$  can be directly used for the generation of the beam spot.

The beam divergences measured with the target are comparable with the angular multiple scattering contribution from each of them (see Sect.2.2). Therefore this contribution must be subtracted from the measured one to obtain the values to be used in generation  $\sigma(s_x) \approx 3.6$  mrad and  $\sigma(s_y) \approx 2.7$  mrad with  $s_{x,y}$  defined in Eq.1. The momentum spread is provided by the DAΦNE staff as  $\sigma(p) = 5.0$  MeV/c.

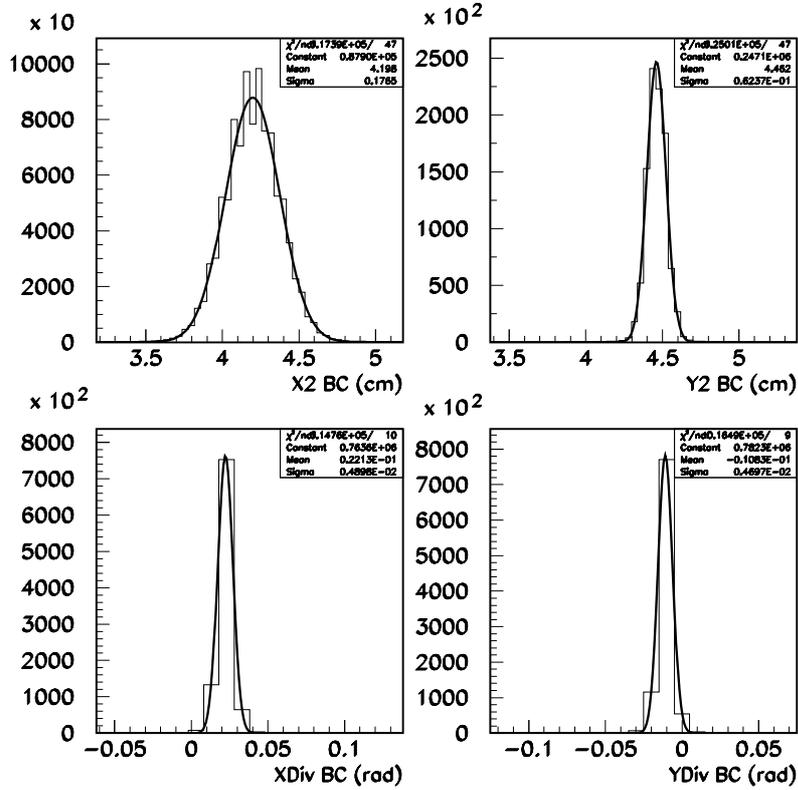


Figure 9: Beam parameters at  $E_e = 463$  MeV measured on a Monte Carlo sample:  $x$  profile (top left),  $y$  profile (top right),  $x$  divergence (bottom left),  $y$  divergence (bottom right).

#### 4.2. The PTS data

The PTS data are those tagging the production of a  $\gamma$  ray directed to the ST and providing an estimation of its energy. Ideally the emission of a bremsstrahlung  $\gamma$  ray from the target would result in an electron hitting the PTS delivering one cluster of neighbouring strips above a predefined threshold. In this case the  $\gamma$ -ray energy would be univocally correlated with the PTS hit position.

The relation between  $\gamma$ -ray energy and PTS hit position, estimated by the cluster centroid, is highly non-linear and must be calibrated. The calibration can be performed either with the help of analytical calculation or relying on Monte Carlo simulations. The former approach cannot easily account for the other interactions of the electron in addition to the bremsstrahlung in the target. Therefore the  $\gamma$ -ray energy,  $E_\gamma$ , is estimated with the PTS energy estimator,  $E_{PTS}$ , calibrated with the Monte Carlo simulations detailed in Sect.4.2.1.

Another important point is the treatment of events with multiple PTS clusters. Ideally these are multi-photon events and should be discarded from the calibration sample. Yet, most of the multi-cluster events are genuine single-photon events where additional clusters are generated by secondary interactions. Furthermore for  $E_\gamma \approx 100$  MeV, the  $e^-$  trajectories intercept PTS detectors on both modules, resulting in high probabilities of multi-cluster events even for single-photon events. Therefore also multi-cluster events are retained.

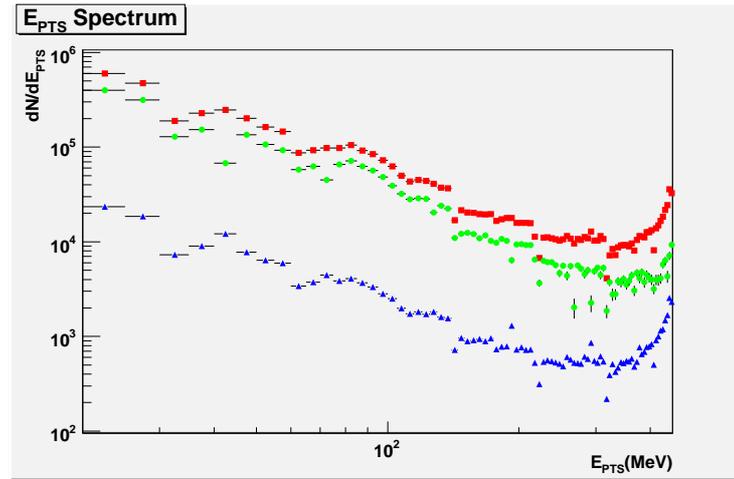


Figure 10: PTS energy spectrum: all events (red squares), only 0- $e^-$  events (blue triangles), normalized difference (green dots).

The spectrum of  $E_{PTS}$  is shown in Fig.10. It displays an anomalous feature at high energy, close to the kinematic limit, where the increase with the energy looks incompatible with the expected behaviour of the bremsstrahlung spectrum in Eq.2.

Two possible explanations are compatible with this excess background: a production of non-bremsstrahlung related low energy electrons entering into the spectrometer or

a photon background in phase with the BTF cycle (the rate of cosmic ray induced hits being too low).

The source of the low energy electrons could be  $\delta$  rays produced in the interaction of the beam electrons with the target. They should be proportional to the number of electrons in the bunch and follow an approximate  $1/E_\delta^2$  spectrum, where  $E_\delta$  is the energy of the  $\delta$  electron. This spectrum would fake a  $1/(E_e - E_\gamma)^2$  spectrum that would qualitatively matches the high energy tail of Fig.10. On the other hand, Monte Carlo simulations and analytical calculations show that this source is largely insufficient to account for the excess of PTS hits corresponding to high  $E_{PTS}$ .

Furthermore the two sources can be discriminated by looking at  $0-e^-$  events, where no PTS hits from beam related  $\delta$  rays are expected. Fig.10 shows a significant fraction of  $0-e^-$  events with PTS hits strongly peaked at high  $E_{PTS}$ , that means at low strip numbers.

Hence only the latter background source is compatible with all experimental data. The existence of a low energy photon background was also confirmed by the accelerator staff.

The spectrum of bremsstrahlung  $\gamma$  rays can be recovered by subtracting the background spectrum appropriately rescaled with the  $0-e^-$  rate but the background events cannot be tagged and removed on a event by event basis.

#### 4.2.1. PTS simulation and comparison with data

In order to provide an interpretation of the PTS data and use them to characterize the PTS/BTF system, a detailed Monte Carlo study is required. The Monte Carlo data contains together with the PTS measurements also the true value at the generation level of the particles (Monte Carlo truth), that can be compared to extract the PTS performances.

A crucial element is the calibration curve relating the PTS cluster position and the electron ( $\gamma$ -ray) energy already used in previous sections. The calibration is obtained looking at Monte Carlo events generated with  $1e^-$  per bunch by plotting the first strip (lowest number) of the first PTS cluster versus  $E_\gamma$ , the energy of the most energetic  $\gamma$  ray as shown in Fig.11(a). This plot is obtained requiring one PTS cluster,  $E_\gamma > 10$  MeV and additional energy from  $\gamma$  rays other than the most energetic one  $< 10$  MeV. The points are distributed along a band plus a small set of outliers, whose origin will be discussed later; in order to use only the points in the band, an additional graphical cut is applied before the 2D histograms is plotted in form of profile histogram. The profile histogram is fitted with a 5-th order polynomial as shown in Fig.11(b). The fit has been also tested on simulated events produced with  $\overline{N}_e = 3.5$  with Poisson distribution, by allowing multiple PTS clusters or by requiring only one  $\gamma$  ray above 100 keV; the fit results are insensitive to the cuts. This functional dependence defines  $E_{PTS}$  as the PTS measured energy. The comparison between the data and Monte Carlo  $E_{PTS}$  distributions is shown in Fig.12. The agreement is reasonable even if some features appear systematically shifted.

#### 4.2.2. PTS inefficiency, false positive and outliers

The fit in Fig.11(b) is obtained using only events where the PTS energy measurement and the true  $\gamma$ -ray energy are significantly correlated. There are events in which

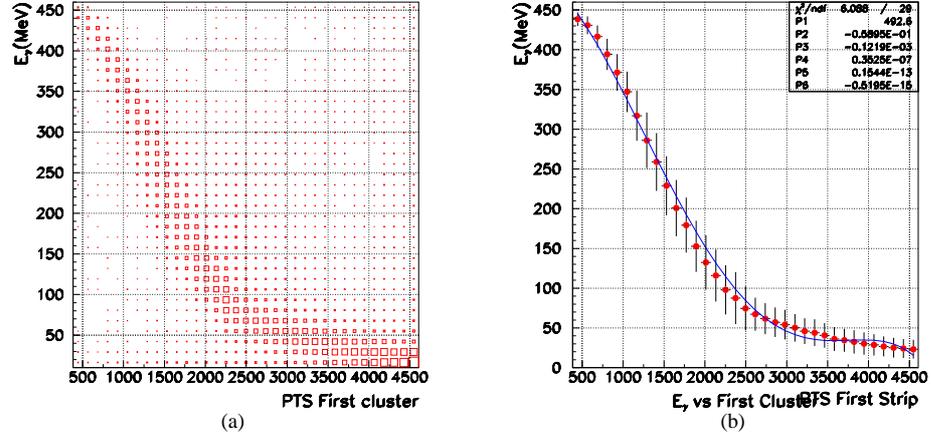


Figure 11:  $E_\gamma$  versus PTS strip number: a) two dimensional b) fitted with 5-th order polynomial.

that is not the case, that can be divided in three broad classes: PTS inefficiency, False positive and Outliers.

#### 4.2.2.1. Inefficiency

The plot  $E_\gamma$  versus  $E_{PTS}$  for Monte Carlo events with 1- $e^-$  per bunch is shown in Fig.13. The PTS inefficiencies, displayed in the vertical line on the left, are events where an electron emits a  $\gamma$  ray by bremsstrahlung but it does not reach the PTS detectors. Such inefficiencies are understood considering the path of an electron inside the 'electron pipe': in absence of a focusing magnet and subject to multiple scattering due to the target (and to the air along the path) the electrons diverge from the ideal trajectory and may hit the wall of the pipe. That is particularly easy along the  $y$  direction where the pipe inner half-height is only 1.75 cm. In this case the  $e^-$  showers and the shower particles ( $e^\pm$ s and photons) may hit or not the PTS detectors.

Another source of inefficiency originates when the  $e^-$  hits the 3.5 mm thick steel inner face of the guide, as expected, and develops a shower fully in the iron. A third cause is due to the  $e^-$  hitting the inner face as expected but the particles exiting from the outer face do not hit the PTS detectors that have an half-height of only 1.00 cm.

#### 4.2.2.2. False positive

The main cause of false positives, that is  $E_{PTS} > 0$  and  $E_\gamma \approx 0$ , is the first reason detailed before to explain inefficiencies: an  $e^-$  that has not emitted a bremsstrahlung  $\gamma$  ray showering in the electron pipe on the top (bottom) face with some particles hitting the PTS detectors. The probability of such events is proportional to the extent of the  $e^-$  divergence and therefore to the  $e^-$  path length. Therefore it should increase almost

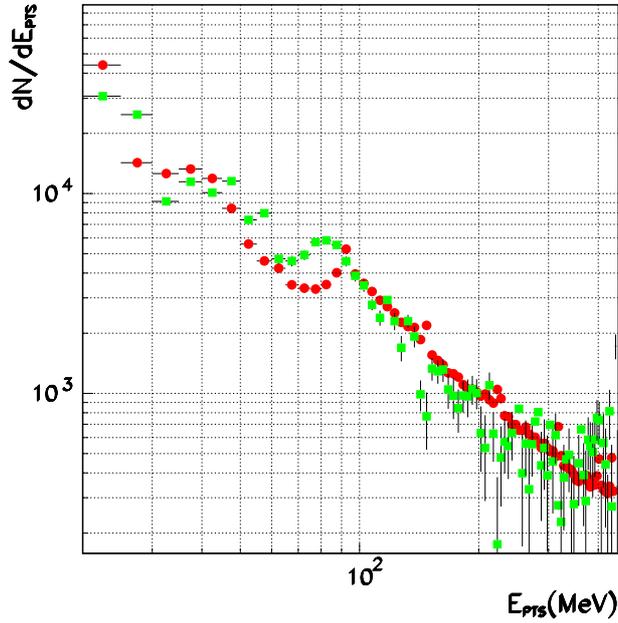


Figure 12: PTS energy spectra for data (green square) and Monte Carlo (red circle)

linearly with the strip number, that is inversely with  $E_{PTS}$ . False positive may also be the results of  $\gamma$  rays actually produced by bremsstrahlung and absorbed along their path in air or by  $e^-$  emitting bremsstrahlung  $\gamma$  rays in air along its path in the electron pipe.

#### 4.2.2.3. Outliers

Outliers are generated by a combination of processes similar to those described above. An  $e^-$  emitting a  $\gamma$  ray and then hitting the top (bottom) face of the pipe and delivering a PTS signal generates an outlier. Outliers can be generated also when the bremsstrahlung  $\gamma$  ray interacts with air creating a  $e^+e^-$  pair, that in turn irradiates a lower energy  $\gamma$  ray such that  $E_\gamma < E_{PTS}$ .

In presence of multiple  $e^-$ s per bunch, a combination of a false positive and of an inefficiency generates an outlier.

Another relevant source is  $e^-$ s that, after having emitted a  $\gamma$  ray, cross the inner face of the pipe showering without delivering a PTS signal close to the crossing point. The shower photons may nevertheless convert in the PTS detectors at higher strip number, so that  $E_{PTS} < E_\gamma$ .

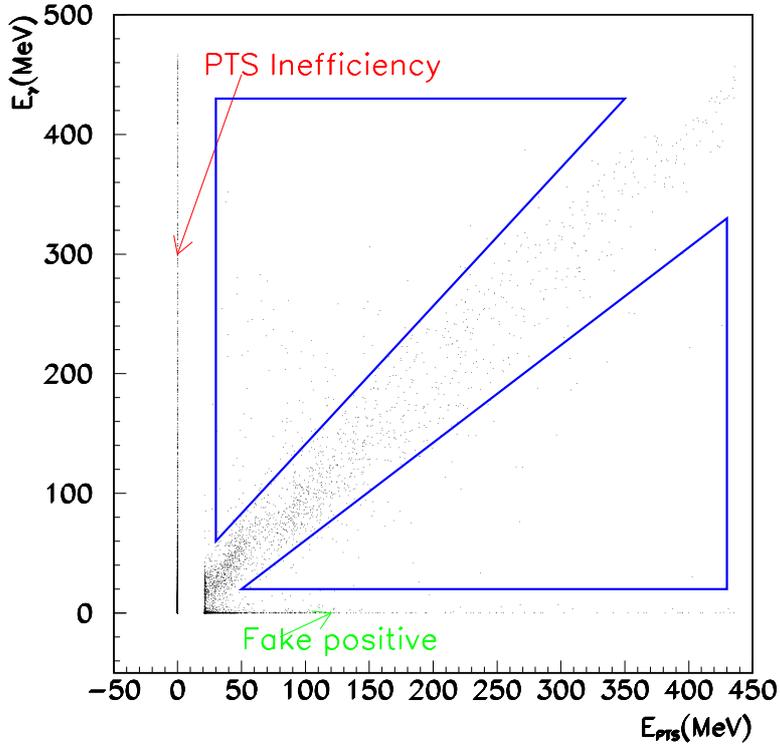


Figure 13:  $E_\gamma$  versus  $E_{PTS}$  scatter plot. The events far from the central band are divided into classes. See text for more details.

#### 4.3. PTS simulation results

Starting from the complex picture previously discussed the PTS can be characterized in different ways. The first step is understanding which is the best requirement on the number of PTS clusters. The possibilities are 1 cluster, 2 clusters and  $\geq 1$  clusters. The first is expected to have low efficiency but also small number of outliers and better energy resolution, the latter has the opposite features while the second is a compromise. In Fig.14 the PTS efficiencies for the three cases are shown. The option with  $\geq 1$  clusters seems to be preferred not only because it has higher efficiency but also because it is less sensitive to the presence of secondary clusters generated by showering particles. In this plot a loose definition of efficiency is used that requires only a PTS cluster regardless of the  $E_{PTS} - E_\gamma$  relation, that is also outliers are included.

The absolute and relative RMS spreads in the  $E_{PTS}$  versus  $E_\gamma$  distribution limited to the central band, that is excluding outliers, are shown in Fig.15(a) and Fig.15(b).

Another approach is looking at the fraction of events with a PTS cluster associated to an energetic  $\gamma$  ray versus  $E_{PTS}$ . That measures the probability of fake positive with

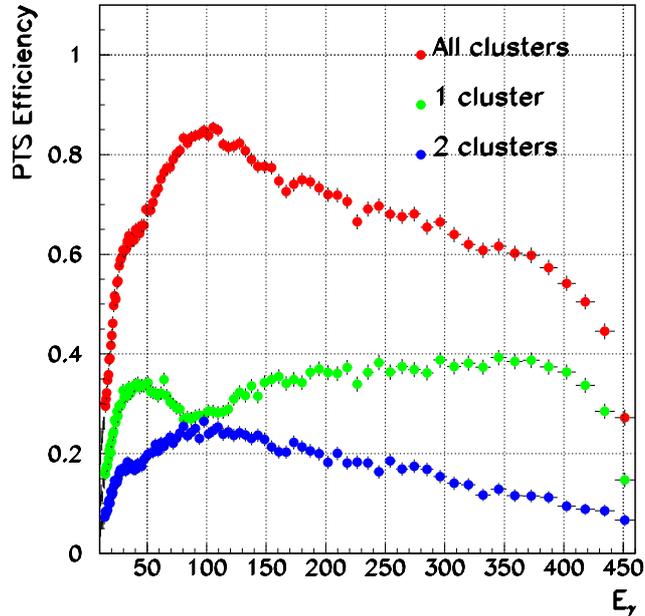


Figure 14: PTS efficiency for events with  $3e^-$  per bunch following Poisson distribution versus  $E_\gamma$ .

the PTS as a photon tagger. A problem with this definition is that there is no infrared limit to  $E_\gamma$ . The lower limit is set by the GEANT threshold for  $\gamma$  production. A more robust definition is to set a threshold defined by the lowest  $E_\gamma$  for which the PTS has a reasonable efficiency, that is  $O(10\text{MeV})$ .

In Fig.16 the probability of having a  $\gamma$  ray above the given threshold versus  $E_{PTS}$  is reported for events with  $\geq 1$  PTS cluster. The complement of this plot gives the fraction of false positive. This fraction is understandably high for low  $E_{PTS}$  where the probability of a non-emitting  $e^-$  hitting the PTS is high and for high  $E_{PTS}$  where the false positives originate from background. For most of the energy range the false positive fraction is  $\leq 10\%$  and weakly dependent on the  $E_\gamma$  threshold.

The absolute and relative RMS spreads in the  $E_\gamma$  versus  $E_{PTS}$  distribution limited to the central band, that is excluding outliers, are shown in Fig.17(a) and Fig.17(b). Outliers constitute at most a few percent of the events and their distribution cannot be easily parameterized.

## 5. Conclusions

The BTF/PTS has been described in detail. It has been characterized by studying the data taken in LNF during the AGILE calibration campaign. Analysis of the target data has allowed to characterize the  $e^-$  beam precisely.

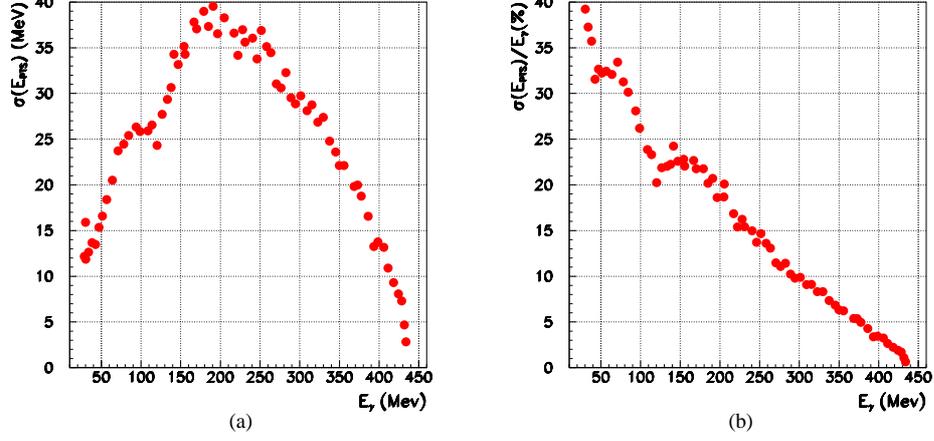


Figure 15: Absolute a) and relative b) spread in  $E_{PTS}$  distribution for events with  $3e^-$  per bunch following Poisson distribution versus  $E_\gamma$ .

The parameters of the Monte Carlo generator have been mostly determined from the data. Corrections to the data have been necessary to account for a background contamination not included in the simulation.

The relation between PTS coordinate and  $\gamma$ -ray energy has been calibrated with the Monte Carlo simulation and the  $E_{PTS}$  distributions from simulation and data are in good agreement.

This calibration of the system allows to use it for calibrating photon detectors, like the ST of AGILE, as presented in a forthcoming paper.

Important parameters of the system like point spread function, effective area and energy resolution versus the  $\gamma$  energy has been extracted through the Monte Carlo simulation validated with this system and used to extract relevant scientific results since the AGILE launch in 2007 [6].

## Appendix

The photon flux can be predicted analytically with some approximated formulae from Quantum Electrodynamics to be compared with the Monte Carlo predictions.

The formula for the bremsstrahlung differential cross-section for photon emission with energy  $E_\gamma$  from an electron with energy  $E_e$  is, with good approximation [11]

$$\frac{d\sigma}{dy} = \frac{A}{X_0 N_A y} \left( \frac{4}{3} - \frac{4}{3}y + y^2 \right) \quad (2)$$

where  $A$  is the atomic number of the material,  $X_0$  its radiation length,  $N_A$  the Avogadro number and  $y = E_\gamma/E_e$ .

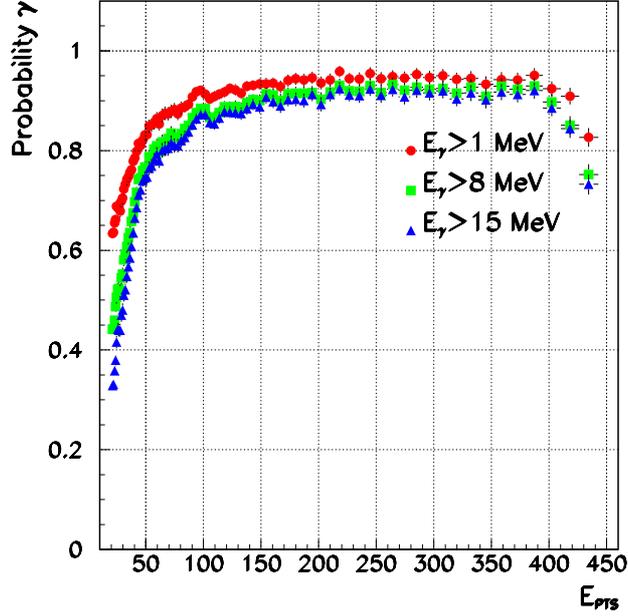


Figure 16: Probability of having  $E_\gamma > 1(8)(15)MeV$  for events with  $3e^-$  per bunch following Poisson distribution versus  $E_{PTS}$ .

Eq.2 can be integrated to predict the number of photons with relative energy between  $y_{min}$  and  $y_{max}$  emitted by a radiator of thickness  $d$

$$\bar{N}_\gamma(y_{min}, y_{max}) = \frac{d}{X_0} \left[ \frac{4}{3} \ln \left( \frac{y_{max}}{y_{min}} \right) - \frac{4}{3} (y_{max} - y_{min}) + \frac{1}{2} (y_{max} - y_{min})^2 \right] \quad (3)$$

In our setup the radiator consists of four silicon layer  $410 \mu m$  thick, a window of Be  $0.5 \text{ mm}$  thick and about  $35.0 \text{ cm}$  of Air.

The total thickness  $d$  expressed in radiation lengths is (with  $X_0^{Air} = 30500.0 \text{ cm}$ ,  $X_0^{Be} = 35.3 \text{ cm}$  and  $X_0^{Si} = 9.36 \text{ cm}$ )

$$\frac{d}{X_0} \approx \frac{35.0 \text{ cm}}{X_0^{Air}} + \frac{0.05 \text{ cm}}{X_0^{Be}} + \frac{4 \times 0.041 \text{ cm}}{X_0^{Si}} \approx 2.0 \cdot 10^{-2}$$

$N_\gamma$  follow the Poisson distribution. Also the number of electrons per bunch follows a Poisson distribution with average  $\bar{N}_e$ , therefore the probability of emitting 1 or more photons is

$$P_{N_e}(N_\gamma = 1) \approx \bar{N}_e \bar{N}_\gamma - (\bar{N}_e \bar{N}_\gamma)^2 \quad (4)$$

$$P_{N_e}(N_\gamma > 1) \approx \frac{(N_e N_\gamma)^2}{2} \quad (5)$$

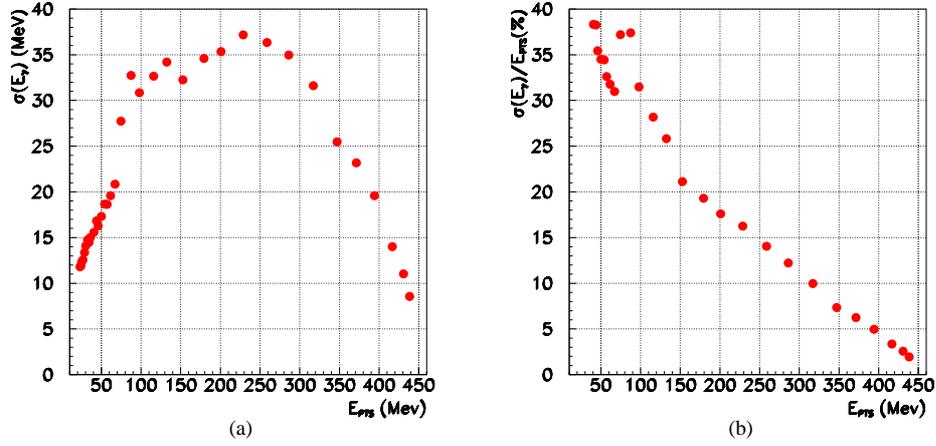


Figure 17: Absolute a) and relative b) spread in  $E_\gamma$  for events with  $3e^-$  per bunch following Poisson distribution versus  $E_{PTS}$ .

## References

- [1] B. Buonomo et al. A tagged photon source at the Frascati beam-test facility (BTF). In *Proceedings of DIPAC 2007, Venice, Italy*, page 63, 2007.
- [2] S. Hasan et al. A Photon Tag Calibration Beam for the AGILE Satellite. LNF-05/24, 2005. Presented at the 9th ICATPP Conference on Astroparticle, Particle, Space Physics, Detectors and Medical Physics Applications, Como, Italy, October 2005.
- [3] G. Barbiellini et al. The AGILE silicon tracker: testbeam results of the prototype silicon detector. *Nuclear Instruments and Methods in Physics Research A*, 490:146, 2002.
- [4] M. Prest et al. The AGILE silicon tracker: an innovative  $\gamma$ -ray instrument for space. *Nucl. Instr. and Meth. A*, 501:280, 2003.
- [5] M. Tavani et al. The AGILE space mission. *Nucl. Instr. and Meth. A*, 588:52, 2008.
- [6] M. Tavani et al. The AGILE mission. *Astron. & Astrophys.*, 502:995–1013, 2009.
- [7] G. Mazzitelli, A. Ghigo, F. Sannibale, P. Valente, and G. Vignola. Commissioning of the DAΦNE beam test facility. *Nucl. Instr. and Meth. A*, 515(3):524 – 542, 2003.

- [8] P.W. Cattaneo et al. First results about on-ground calibration of the silicon tracker for the agile satellite. *Nucl. Instr. and Meth. A*, 630(1):251 – 257, 2011. Proceedings of the 2nd Roma International Conference on Astroparticle Physics (RICAP 2009).
- [9] B. Buonomo, G. Mazzitelli, and P. Valente. Performance and upgrade of the DAΦNE beam test facility. In *IEEE Nuclear Science Symposium Conference Record, Rome, Italy*, October 2004.
- [10] G. Mazzitelli, B. Buonomo, L. Quintieri, and P. Valente. The DAΦNE Beam Test Facility: from 1 to 10 milliards of particles. In *Proceedings of EPAC 2006, Edinburgh, Scotland*, 2006.
- [11] W.M. Yao et al. Review of Particle Physics. *Journal of Physics G*, 33, 2006.
- [12] R. Brun et al. *GEANT3-Detector Description and Simulaton Tool, CERN Program Library Long Writeups W5013*, 1993.
- [13] P.W. Cattaneo. Capacitance calculation in a microstrip detector and its application to signal processing. *Nucl. Instr. and Meth. A*, 295:207–218, 1990.